

DOI: 10.1002/ ((please add manuscript number))

Article type: Full paper

Ultrathin high surface area nickel boride (Ni_xB) nanosheets as highly efficient electrocatalyst for oxygen evolution

Justus Masa^{}, Ilya Sinev, Hemma Mistry, Edgar Ventosa, Maria de la Mata, Jordi Arbiol, Martin Muhler, Beatriz Roldan Cuenya, Wolfgang Schuhmann^{*}*

Dr. J. Masa, Dr. E. Ventosa, Prof. Dr. W. Schuhmann.

Analytical Chemistry – Center for Electrochemical Sciences (CES), Ruhr Universität Bochum, D-44780 Bochum (Germany)

E-mail: justus.masa@rub.de, wolfgang.schuhmann@rub.de

Dr. I. Sinev, Dr. H. Mistry, Prof. Dr. Beatriz R. Cuenya

Department of Physics, Ruhr-University Bochum, D-44801 Bochum (Germany)

Dr. H. Mistry

Department of Physics, University of Central Florida, Orlando, FL 32816, USA

M. de la Mata, Prof. J. Arbiol

Catalan Institute of Nanoscience and Nanotechnology (ICN2), CSIC, and The Barcelona Institute of Science and Technology (BIST), Campus UAB, Bellaterra, 08193 Barcelona, Catalonia, Spain

Prof. J. Arbiol

This is the author manuscript accepted for publication and has undergone full peer review but has not been through the copyediting, typesetting, pagination and proofreading process, which may lead to differences between this version and the [Version of Record](#). Please cite this article as [doi: 10.1002/aenm.201700381](#).

This article is protected by copyright. All rights reserved.

ICREA, Pg. Lluís Companys 23, 08010 Barcelona, Catalonia, Spain

Prof. Dr. M. Muhler

Laboratory of Industrial Chemistry, Ruhr-University Bochum, D-44801 Bochum (Germany)

Keywords: nickel boride, water oxidation, water splitting, hydrogen evolution, oxygen evolution, XAFS

The overriding obstacle to mass production of hydrogen from water as the premium fuel for powering our planet is the frustratingly slow kinetics of the oxygen evolution reaction (OER). Additionally, inadequate understanding of the key barriers of the OER is a hindrance to insightful design of advanced OER catalysts. Herein, we present ultrathin amorphous high-surface area nickel boride (Ni₃B) nanosheets as a low-cost, very efficient and stable catalyst for the OER for electrochemical water splitting. The catalyst afforded 10 mA cm⁻² at 0.38 V overpotential during OER in 1.0 M KOH, reducing to only 0.28 V at 20 mA cm⁻² when supported on nickel foam, which ranks it among the best reported non-precious catalysts for oxygen evolution. *Operando* XAFS measurements revealed prevalence of NiOOH, as well as Ni-B under OER conditions, owing to a Ni-B core@nickel oxyhydroxide shell (Ni-B@NiO_xH) structure, and increase in disorder of the NiO_xH layer, thus revealing important insight into the transient states of the catalyst during oxygen evolution.

Electrochemical water splitting for hydrogen production is impeded by intensive energy consumption mostly due to the slow kinetics of the oxygen evolution reaction (OER), and the

This article is protected by copyright. All rights reserved.

Author Manuscript

requirement to use costly and rare platinum group metal (PGM) catalysts, rendering the process of low economic appeal^[1]. Efforts to reduce or completely substitute the use of PGM electrocatalysts (Pt, IrO₂ and RuO₂), the state-of-the-art catalysts for electrochemical water splitting (ECWS), with less costly alternatives to leverage the competitiveness of ECWS have been futile in the past^[2]. Moreover, even with Pt as the cathode, and RuO₂ or IrO₂ as the anode, large overpotentials are still incurred to achieve meaningful electrolysis rates^[3]. ECWS using non-precious metal catalysts is more promising in high pH electrolytes, where Ni, Co and Fe-based materials are very promising^[4]. Specifically, mixed metal oxides and hydroxides^[5,6,7], and compounds of Co and Ni incorporating non-metal elements, typically, B, N, S, Se and P^[8], have proved phenomenal in alkaline water oxidation, with activities surpassing RuO₂ and IrO₂ being reported for NiSe, Ni₅P₄, Ni₂P, CoP, Ni₃N, among others. Meanwhile, binary and ternary compounds of Co, Fe, Mo, W, and Ni with B, P, S, and Se, among others, also exhibit outstanding activity in catalyzing the hydrogen evolution reaction (HER)^[9,10]. These developments inspire new directions in the search for advanced non-precious catalysts for ECWS. For electrochemical applications, high surface area materials either with a layered structure or high porosity^[10,11], but most preferably those which combine both of these properties, are desirable owing to their high active site densities, which favour a high active site utilization.

Herein, we report the synthesis of ultrathin high surface area amorphous nickel boride (Ni_xB) nanosheets and demonstrate their remarkable activity and stability as non-precious metal catalyst for oxygen evolution under alkaline conditions. The catalyst afforded 10 mA cm⁻² at 0.38 V overpotential during OER in 1.0 M KOH, which reduced to only 0.28 V at 20 mA cm⁻² when supported on nickel foam. Additionally, we present insight from *operando* XAFS of the nature of transient

This article is protected by copyright. All rights reserved.

states of the catalyst during oxygen evolution. The active form of the catalyst is a Ni-B@NiOOH (core@shell) structure. We observed a contraction of the Ni-O bonds in NiOOH accompanied with increase in disorder of the layer, and very fast deoxygenation of the terminal intermediate during active oxygen evolution.

Nickel boride (Ni_xB) was prepared by chemical reduction of nickel ions in a deaerated 1.0 M $\text{NiCl}_2 \cdot 6\text{H}_2\text{O}_{(\text{aq})}$ solution using 1.0 M $\text{NaBH}_{4(\text{aq})}$ (See SI for details). The composition of Ni and B in the product was 76.2 % and 6.6 % respectively, corresponding to a Ni:B stoichiometry of 2:1 (**Table S1**), the rest being mostly oxygen (**Figure S1**). X-ray diffraction (XRD) studies (**Figure 1**) revealed Ni_xB to be XRD amorphous. The product remained XRD amorphous upon annealing under Ar at 300 °C for 2 h. Further increase of the annealing temperature to 600 °C led to crystallization and emergence of Ni_3B (ICSD: 614985) as the major phase, and Ni_2B (ICSD 75792) as a minor phase. Ni_3B remained the dominant phase in the sample annealed at 1000 °C, with minor reflections assignable to Ni_2B also detectable. Structure refinement using Rietveld analysis revealed that Ni_xB -1000 contained 79% Ni_3B while Ni_2B made up 21%. Ni_xB annealed at 300 °C (Ni_xB -300) exhibited the best electrochemical performance (discussed later) and was thus characterized in more detail.

Ni_xB -300 comprised of very thin sheets as well as discrete particles (**Figure 1b**). High resolution TEM (HRTEM) analysis of an individual flake of Ni_xB -300 (**Figure 1c**) reveals atomically thin layers with a thickness of about 6.6 Å (**Figure 1d**).

AFM images of Ni_xB -300 recorded in the tapping mode and the corresponding height profile (**Figure S3**) revealed that the individual nanosheets were predominantly about 1.0 nm thick, with lateral dimensions in the range of ~ 200 – 300 nm.

This article is protected by copyright. All rights reserved.

Spectroscopic analysis by electron energy loss spectroscopy (EELS) shows that the discrete particles are predominantly nickel boride, while the sheets have a uniform distribution of Ni, B, as well as oxygen (**Figure S3**). Fast Fourier Transform (FFT) analysis of selected regions of the HRTEM images disclosed predominance of Ni₂B nanocrystallites in Ni_xB-300 (**Figure S4**). Crystallites of Ni₃B were also occasionally found (**Figure 1e**). In consideration of the XRD and TEM observations, it can be concluded that Ni_xB-300 was composed of nanocrystallites of Ni₂B, and Ni₃B to a less a less extent, as well as very small particles of Ni⁽⁰⁾. The predominance of the Ni₃B phase at high annealing temperatures, as confirmed by XRD, indicates thermally induced transition of Ni₂B to Ni₃B, and also suggests the reaction of Ni with Ni₂B to form Ni₃B (Ni + Ni₂B → Ni₃B), consistent with the work by Glavee et al.^[12] among others.

XPS examination of the chemical state of as prepared Ni_xB minimally exposed to air showed the main Ni 2p_{3/2} and Ni 2p_{1/2} core peaks at 852.5 eV and 869.6 eV (**Figure 2a(i)**), respectively, typical of Ni₂B^[13]. The Ni 2p_{3/2} and Ni 2p_{1/2} satellite peaks at 855.6 eV and 873.0 eV, respectively, are due to Ni²⁺, indicating the presence of surface oxide or hydroxide species. Amorphous metal borides are spontaneously oxidized when exposed to air and water to form surface oxides/hydroxides leading to a core@shell (metal boride@metal oxide/hydroxide) structure^[14]. Ni_xB exposed to air, (**Figure 2a(ii)**), thus exhibited a predominantly oxidized surface with a dominant Ni 2p_{3/2} peak at 855.82 eV (Ni²⁺ species) and minor peak at 852.52 eV due to the interaction of nickel with boron (**Figure 2a**).

A positive chemical shift of 0.95 eV in the binding energy of the Ni 2p_{3/2} peak was observed upon annealing Ni_xB at 300 °C (**Figure 2c**), indicating relative displacement of electrons from nickel. The

This article is protected by copyright. All rights reserved.

annealing process thus led to modification of the surface electronic structure of Ni_xB-300, which had a beneficial effect on its OER activity.

The B 1s spectrum of as prepared Ni_xB minimally exposed to air (Ni_xB-(i) in **Figure 2b**) was deconvoluted into two distinct species at 187.9 eV and 191.8 eV (**Figure 2b**). The species at 187.9 eV is due to interaction of boron with nickel, whereas the one at 191.8 eV is due to boron-oxo species. On the other hand, the B 1s spectrum of Ni_xB exposed to air for several hours (Ni_xB-(ii) in **Figure 2b**) was deconvoluted into two contributions at 190.07 eV and 192.0 eV both corresponding to boron oxide species. The O 1s spectrum of Ni_xB-300 (**Figure 2d**), not activated sample, shows that its surface was covered with Ni(OH)₂. Meanwhile, after electrochemical activation (activated in **Figure 2d**), which involved 50 cycles of potential cycling in 1.0 KOH between 0.95 V and 1.65 V vs RHE, the surface was mainly covered with a nickel oxyhydroxide (NiOOH) layer.

X-ray absorption fine-structure spectroscopy (XAFS) measurements were carried out on Ni_xB, Ni_xB-300 and Ni_xB-1000 to probe the influence of annealing temperature on the chemical state and local coordination structure of the catalyst. X-ray absorption near edge structure (XANES) spectra are presented in **Figure 3(a)**. The pre-edge region of Ni_xB and Ni_xB-300 consist of a small peak at ca. 8327.2 eV whose shape and position match very well with Ni(OH)₂ and NiO (not shown) reference spectra. The first feature above the absorption edge (white-line) centred at 8344.6 eV, is also in agreement with the NiO and Ni(OH)₂ spectra, thus indicating predominance of the Ni²⁺ state in the samples. On the other hand, the XANES spectrum of Ni_xB-1000 shows close resemblance to a commercial nickel boride reference (Sigma Aldrich), featured by a white line significantly less intense than the Ni²⁺ references. In this case, the XANES results are in good agreement with XRD data described before. However, the reference nickel boride sample, NiB (Sigma-Aldrich) was composed

This article is protected by copyright. All rights reserved.

of several distinct Ni_xB_y phases and was thus not a suitable reference for discussion of the EXAFS data following hereafter.

Extended X-ray absorption fine-structure (EXAFS) spectra of Ni_xB , $\text{Ni}_x\text{B-300}$ and $\text{Ni}_x\text{B-1000}$ (**Figure 3b**) reveal significant differences induced by the annealing processes on the local environment of nickel. The shape of both Ni_xB and $\text{Ni}_x\text{B-300}$ spectra show the presence of backscattering events characteristic of Ni^{2+} compounds, namely Ni-O at 2.07 Å and Ni-Ni at 3.1 Å (uncorrected for phase shift). There is an extra peak emerging at 2.2 Å (uncorrected) on the EXAFS spectrum of the sample annealed at 300°C indicating the presence of B in a local Ni environment. Moreover, peak separation of the spectrum for the untreated Ni_xB sample with a plateau between 2.1 and 2.3 Å gives hint of a similar Ni-B coordination. Detailed analysis of the EXAFS spectra performed by fitting a combination of Ni-O, Ni-B and Ni- Ni^{2+} backscattering paths to the spectral features described above, gives proof to the hypothesis of the presence of boron as nearest neighbour in Ni local coordination (see **Table S2** for details). Thus, in the as prepared Ni_xB sample, the effective Ni-B coordination number is as low as 1.8, while a high value of the corresponding σ^2 ($11.9 \cdot 10^{-3} \text{ \AA}^2$) indicates significant disorder in the boride structure. Annealing at 300 °C results in an increase of the Ni-B coordination number to 4.2, and ordering of the boride structure with a less ordered $\text{Ni}(\text{OH})_2$ phase evidenced by a lower Ni- Ni^{2+} coordination number and higher σ^2 . The EXAFS spectrum of $\text{Ni}_x\text{B-1000}$ is dominated by a peak at 2.05 Å (uncorrected), and can be fitted for the most by Ni-B and a minor amount of Ni-O. The Ni-B coordination number as high as 13.4 in this case can be interpreted by overlapping of several Ni-B backscattering events from different well-ordered Ni_xB_y phases, as indicated by XRD.

A film of Ni_xB was adsorbed on a glassy carbon electrode and investigated for electrocatalysis of OER in 0.1 M KOH (See SI for details of film preparation). Before

This article is protected by copyright. All rights reserved.

acquiring any electrochemical data, the electrode was first subjected to continuous potential cycling at a scan rate of 0.1 V s^{-1} between 0.95 to 1.65 V (RHE) until reproducible voltammograms were obtained (**Figure 4a**). The continuous increase in the intensity of both the anodic and cathodic peaks centred at about 1.40 V is due to growth of a NiOOH layer (**Figure 2d**). The anodic process is due to oxidation of Ni^{2+} to Ni^{3+} , while the reverse process is the reduction of Ni^{3+} back to Ni^{2+} , that is, $\text{Ni}(\text{OH})_2 + \text{OH}^- \leftrightarrow \text{NiOOH} + \text{H}_2\text{O} + \text{e}$. Results for electrocatalysis of the OER by Ni_xB in 0.1 M KOH are presented in **Figure 4b**. The OER activity of Ni_xB became enhanced upon annealing in argon for 2 hours, reaching a maximum at 300 °C followed by a drastic decline at higher annealing temperatures. The catalyst was not able to attain 10 mA cm^{-2} within the investigated potential window (1.0 - 1.8 V) when annealed at or above 700 °C. The inset of **Figure 4b** shows variation of the OER activity of Ni_xB with annealing temperature, expressed as the potential corresponding to a current density of 10 mA cm^{-2} . The non-annealed sample, Ni_xB , attained 10 mA cm^{-2} at 1.73 V, while $\text{Ni}_x\text{B-200}$ and $\text{Ni}_x\text{B-300}$ afforded 1.68 and 1.61 V, respectively, at the same current density. Importantly, $\text{Ni}_x\text{B-300}$ exhibited better OER activity than $\text{Ni}_x\text{B-200}$ despite the former possessing a slightly lower BET surface area, $122.3 \text{ m}^2 \text{ g}^{-1}$ for $\text{Ni}_x\text{B-300}$ versus $127.4 \text{ m}^2 \text{ g}^{-1}$ for $\text{Ni}_x\text{B-200}$ (**Table S1**). This implies that increase of the OER activity from Ni_xB through $\text{Ni}_x\text{B-200}$ and $\text{Ni}_x\text{B-300}$, cannot be explained in terms of surface area.

It is worth to note that the intensity of the $\text{Ni}^{2+} \leftrightarrow \text{Ni}^{3+}$ redox peaks followed a trend exactly similar to the OER activity dependence on temperature. Characteristically, the area under the $\text{Ni}^{2+} \leftrightarrow \text{Ni}^{3+}$ redox peaks is proportional to the amount of electrochemically addressable nickel atoms/ions, which is intimately linked to conductivity. The observed enhancement of

This article is protected by copyright. All rights reserved.

the OER activity with annealing temperature is thus mainly attributed to increase of the electrical conductivity of the catalyst due to sintering of the catalyst particles. Besides affecting the geometrical properties, XPS analysis revealed that the annealing process also induces changes in the chemical state of the catalyst surface ascribed to electronic structure modification. For example, a positive chemical shift in the BE of the Ni 2p_{3/2} peak of 0.95 eV, from 852.4 eV to 853.5 eV, was observed when Ni_xB was annealed at 300 °C (**Figure 2c**). The decline in activity at much higher annealing temperatures is certainly due to decrease of the surface area due to the growth in particle size. The BET surface area decreased from 122.3 m² g⁻¹ for Ni_xB-300 to 16.3 m² g⁻¹ for Ni_xB-600, and to 7.9 m² g⁻¹ for Ni_xB-1000.

Galvanostatic stability measurements of Ni_xB-300 supported on a graphite RDE electrode at a current density of 10 mA cm⁻² in 0.1 M KOH indicate very stable performance of the catalyst with essentially no loss in performance after 60 h (**Figure 4c**). The Faraday efficiency, determined using the rotating ring-disk electrode (RRDE) technique^[15], was 98.9 % (Figure S11), indicating the applied current was nearly exclusively used for oxygen evolution. In metal borides, the boron atoms are capable of forming linear, planar and three-dimensional structures surrounded by metals,^[6,16] through the formation of covalent M-B, as well as B-B bonds, making these compounds extremely hard and chemically resistant.

Nickel foam is an attractive 3D catalyst support for gas evolution electrodes owing to its high surface area, stability and synergistic catalytic effect.^[6,17,17,18] We supported Ni_xB-300 on nickel foam (Ni_xB-300/NF) and investigated the resulting electrodes for the OER in a custom-built flow-through cell^[19]. Figure 5a shows the OER performance of the Ni_xB-300/NF electrode in 0.1 M KOH compared to Ni_xB-

This article is protected by copyright. All rights reserved.

300 supported on glassy carbon (Ni_xB-300/GC), and bare NF. Employing NF as a support led to tremendous increase of the current and significant reduction of the overpotential. In our case, it was not valid anymore to extract the potential corresponding to a current density of 10 mA cm⁻² since this overlapped with the gigantic Ni²⁺ → Ni³⁺ + e⁻ oxidation wave. A current density of 20 mA cm⁻² (normalized to geometric electrode area) was attained at an overpotential of only 0.28 V. To benchmark the performance of Ni_xB-300, its activity was compared against some recently reported highly active non-precious OER catalysts, particularly, nickel-based catalysts supported on nickel foam (**Table S3**). As an example, a NiFe double layer hydroxide doped with nitrogen (N-NiFe-LDH) directly grown on nickel foam afforded 0.23 V overpotential at a current density of 10 mA cm⁻² in 0.1 M KOH^[20]. A NiCoP catalyst supported on nickel foam delivered a current of 10 mA cm⁻² at an overpotential of 0.28 V in 1.0 M KOH^[21]. A gelled material comprised of a ternary homogeneous mixture of Fe, Co and W oxyhydroxides delivered a current density of 10 mA cm⁻² at an overpotential of 0.19 V during OER in 1.0 M KOH^[22]. A recently reported cobalt phosphide Co/Co₂P oxygen evolution catalyst supported on nickel foam afforded 50 mA cm⁻² at only 0.19 V overpotential^[23]. The performance of Ni_xB-300 is thus clearly very promising and among the best reported for nickel based catalysts. Importantly, Ni_xB-300 required the same potential (0.38 V) to deliver 10 mA cm⁻² as RuO₂ and IrO₂ (**Figure S12**). The Tafel slope of Ni_xB-300 $\left(\frac{\partial E}{\partial(\ln i)}\right)$, derived from Figure 4b, was 89 mV/dec, while that for OER on RuO₂ was 88 mV/dec and 90 mV/dec on IrO₂. The Tafel slopes of the OER are essentially similar and suggest that the rate limiting step on these catalysts is a coupled chemical-charge transfer step^[24]. The turnover frequency (TOF) of oxygen evolution, calculated with respect to the total estimated amount of Ni in the catalyst (Ni = 79.1 %, ICP-MS data), at 1.60 V (0.37 V overpotential), was ~0.048 s⁻¹ on Ni_xB-300, whereas it was and ~0.098 s⁻¹ on RuO₂. Therefore, since

This article is protected by copyright. All rights reserved.

the TOF is an intensive catalytic parameter, the results show that RuO₂ was potentially more active than Ni_xB-300 on a per active site basis despite the catalysts exhibiting a similar overpotential at 10 mA cm⁻². Ni_xB-300 thus evidently benefitted from its high surface area, 122 m² g⁻¹ compared to 1.2 m² g⁻¹ for RuO₂, which facilitated a higher catalyst utilization.

The chemical state and structure of the catalyst under OER conditions was probed via *operando* XAFS studies. **Figure 5** presents overlaid *operando* XANES (a) and EXAFS (b) spectra of Ni_xB-300 after electrochemical conditioning between 1.0 V and 1.6 V, during polarization at 1.0 V, a potential below the redox transition from Ni²⁺ (Ni(OH)₂) to Ni³⁺ (NiOOH), and at 1.7 V, a potential at which oxygen evolution takes place. The XANES spectra of the pre-conditioned sample and during the polarization at 1.0 V do not show any differences compared to the initial state. Under OER conditions, the Ni-K edge position remains unchanged as well, although there are clear changes in both the slope and specific features of the spectrum. The spectrum measured at 1.7 V has a lower white line intensity with its maximum shifted to higher energy. It resembles the spectrum of NiOOH, produced by *in-situ* electrochemical oxidation of Ni(OH)₂ at 1.6 V_{RHE} and is also similar to the spectra of Ni³⁺ species reported in the literature^[25,26]. This change observed under reaction conditions indicates that there was a change in the oxidation state from Ni²⁺ to Ni³⁺ (NiOOH) taking place under OER conditions^[25,26]. The EXAFS spectra measured under *operando* conditions resemble well those of Ni_xB-300 measured *ex-situ*, showing the presence of both Ni(OH)₂ structure (peaks at 1.55 and 2.73 Å corresponding to Ni-O and Ni-Ni²⁺ backscattering), and Ni-B in the first coordination sphere represented by a small peak at 2.15 Å (all uncorrected for a phase shift). The fitted Ni-O distance does not change after the electrochemical cycling pre-treatment as compared to the untreated sample, but reduces first to 2.05 Å at 1.0 V and then to 2.03 Å at 1.7 V (see **Table S4**). At the same time, the corresponding

This article is protected by copyright. All rights reserved.

coordination numbers decrease from 3.7 to 3.3 and 3.0 for the pre-conditioned sample, and during polarization at 1.0 V and at 1.7 V, respectively. The Ni-Ni²⁺ coordination number changes drastically from 5.7 to 4.0 when comparing the prepared sample to that measured under operando conditions at 1.7 V. The changes observed in the EXAFS features, associated with the Ni²⁺ state can have twofold explanation. Firstly, the significant change of coordination number in the Ni-Ni²⁺ backscattering pair compared to Ni-O points to a less ordered structure under harsh OER conditions since the more distant coordination shells are more sensitive to a material's long range order. Another explanation is associated with the chemical state changes observed on the XANES spectra. Both Ni(OH)₂ and NiOOH structures form Ni-O as well as Ni-Ni^{X+} (X = 2, 3) backscattering signals, however shifted by ca. 0.3 Å towards shorter distances in the case of Ni³⁺. When both structures are present in the sample, the corresponding photoelectron waves interfere destructively due to phase mismatch. This hypothesis is supported by the apparent contraction of the Ni-O bond observed at 1.7 V_{RHE}, consistent with observations by other groups^[7,27].

In the abridged mechanism of O₂ evolution,^[28] involving the reaction sequence: (i) $M + OH^- \rightarrow MOH + e^-$; (ii) $MOH + OH^- \rightarrow MO + H_2O + e^-$; (iii) $MO + OH^- \rightarrow MOOH + e^-$; (iv) $MOOH + OH^- \rightarrow MO_2 + H_2O + e^-$; and (v) $MO_2 \rightarrow M + O_2$, equations (i) to (iii) all involve growth of an oxide layer. In (i) and (ii), Ni is present as Ni²⁺, while (iii) involves Ni²⁺ to Ni³⁺ transition, and in (iv) Ni³⁺ is oxidized to Ni⁴⁺. Based on this mechanism, a fingerprint of Ni⁴⁺ should be trackable under active oxygen evolution conditions using a suitable *operando* technique^[27]. By employing *pseudo-operando* XAFS, and other complementary *in-situ* techniques to track the redox states of Ni and Fe in a Ni-Fe(OOH) catalyst, Strasser et al.^[27,29] observed that, for a low content of Fe in the catalyst, < 4%, Ni⁴⁺ was the dominant redox state of Ni under catalytic OER conditions. Conversely, a high Fe content, > 4%,

This article is protected by copyright. All rights reserved.

stabilized the Ni²⁺ state thereby suppressing the higher-valent states of Ni (Ni³⁺ and Ni⁴⁺) under catalytic O₂ evolution conditions, resulting in faster oxygen evolution kinetics at the expense of the oxidation of Ni²⁺. The authors concluded based on these observations, that Ni²⁺Fe³⁺OOH, is the active state of the Ni-Fe(OOH) catalyst under catalytic conditions. For bulk electrode materials, the OER takes place on a thin surface oxide-hydroxide layer making it challenging to observe the transient states of OER catalysts whose bulk properties predominate the surface properties by employing an averaging technique. The Ni_xB-300 catalyst probed here comprised of ultrathin sheets of atomic scale thickness ($\approx 6.6 \text{ \AA}$), with a core-shell (Ni-B@NiO_x) structure, where the surface properties (Ni²⁺) predominated the core properties (Ni-B), as demonstrated by XAFS in **Figure 3**, which makes the catalyst suitable for *operando* XAFS studies. Our *operando* XAFS studies did not disclose any features attributable to the Ni⁴⁺ state at active O₂ evolution potentials. To rationalize this observation on the premise of the mechanism outlined above, deoxygenation of the NiO₂ intermediate, step (v) has to be comparatively faster in relation to the other reaction steps. Interestingly, our observations lead to a conclusion which appears to be coherent with the work of Strasser et al.^[27,29]. Our findings there present new insights into the dynamics of OER catalyst structures under reaction conditions, as well as the dynamics of some transient states of the catalyst during the OER.

Nickel boride (Ni_xB) comprised of very thin sheets and small nanoparticles with a Ni-B core and nickel hydroxide shell (Ni-B@Ni(OH)₂) structure is unveiled as a highly efficient and stable electrocatalyst for oxygen evolution under alkaline conditions. When supported on nickel foam, the catalyst drives the OER at 20 mA cm⁻² at only 0.28 V overpotential in 1.0 M KOH. We observed by *operando* XAFS, intactness of the Ni-B core under active oxygen evolution, and simultaneously, a transition of Ni²⁺ to Ni³⁺ (NiOOH) in the shell leading to shortening of Ni-O bonds and increase in disorder of the nickel

This article is protected by copyright. All rights reserved.

oxyhydroxide layer. The synthesis of nickel boride is simple and readily scalable, making it a very attractive and competitive non-precious anode catalyst in ECWS for mass hydrogen production.

Supporting Information

Supporting Information is available from the Wiley Online Library or from the author.

Acknowledgements

The authors are grateful to Mr. Daniel Peters for support with XRD measurements and interpretation, Dr. Wei Xia and Dr. Christoph Somsen for initial TEM analysis and interpretation, Mrs. Sandra Schmidt for SEM measurements, and Mr. Martin Trautmann for the AFM measurements. Staff of beamlines 2-2 (Stanford Synchrotron Radiation Lightsource), ID10 (Advanced Photon Source) and SAMBA (SOLEIL) are acknowledged for their support during XAFS measurements. This work was made possible thanks to the financial support from the US National Science Foundation (NSF-Chemistry 1213182) and the Cluster of Excellence RESOLV at RUB (EXC 1069) funded by the Deutsche Forschungsgemeinschaft. BRC and IS gratefully acknowledge financial support from the German Federal Ministry of Education and Research (Bundesministerium für Bildung und Forschung, BMBF) under grant #03SF0523C, CO2EKAT. MRCAT operations are supported by the Department of Energy and the MRCAT member institutions. This research used resources of the Advanced Photon Source, a U.S. Department of Energy (DOE) Office of Science User Facility operated for the DOE Office of Science by Argonne National Laboratory under Contract No. DE-AC02-06CH11357. Use of the Stanford Synchrotron Radiation Lightsource, SLAC National Accelerator Laboratory, is supported by the U.S. Department of Energy, Office of Science, Office of Basic Energy Sciences under Contract No. DE-AC02-76SF00515. MdIM and JA acknowledge funding from Generalitat de Catalunya 2014 SGR 1638 and the Spanish MINECO coordinated projects between IREC and ICN2 TNT-FUELS and e-TNT and ICN2 Severo Ochoa Excellence Program.

This article is protected by copyright. All rights reserved.

Received: ((will be filled in by the editorial staff))

Revised: ((will be filled in by the editorial staff))

Published online: ((will be filled in by the editorial staff))

References

- [1] a) F. Barbir, *Solar Energy* **2005**, *78*, 661; b) K. Zeng, D. Zhang, *Prog. Energ. Combust* **2010**, *36*, 307.
- [2] C. C. L. McCrory, S. Jung, I. M. Ferrer, S. M. Chatman, J. C. Peters, T. F. Jaramillo, *J. Am. Chem. Soc.* **2015**, *137*, 4347.
- [3] T. Reier, M. Oezaslan, P. Strasser, *ACS Catal.* **2012**, *2*, 1765.
- [4] Y. Xu, W. Tu, B. Zhang, S. Yin, Y. Huang, M. Kraft, R. Xu, *Adv. Mater.* **2017**. DOI: 10.1002/adma.201605957.
- [5] a) L. J. Enman, M. S. Burke, A. S. Batchellor, S. W. Boettcher, *ACS Catal.* **2016**, *6*, 2416; b) M. S. Burke, M. G. Kast, L. Trotochaud, A. M. Smith, S. W. Boettcher, *J. Am. Chem. Soc.* **2015**, *137*, 3638; c) M. Gong, Y. Li, H. Wang, Y. Liang, J. Z. Wu, J. Zhou, J. Wang, T. Regier, F. Wei, H. Dai, *J. Am. Chem. Soc.* **2013**, *135*, 8452; d) F. Song, X. Hu, *Nat. Commun.* **2014**, *5*, 4477; e) W. Zhang, Y. Wu, J. Qi, M. Chen, R. Cao, *Adv. Energy Mater.* **2017**, 1602547; f) Y. Zhu, W. Zhou, Y. Zhong, Y. Bu, X. Chen, Q. Zhong, M. Liu, Z. Shao, *Adv. Energy Mater.* **2016**, 1602122.
- [6] X. Lu, C. Zhao, *Nat. Commun.* **2015**, *6*, 6616.
- [7] F. Dionigi, P. Strasser, *Adv. Energy Mater.* **2016**, *6*, 1600621.
- [8] M. Sun, H. Liu, J. Qu, J. Li, *Adv. Energy Mater.* **2016**, *6*, 1600087.
- [9] a) E. J. Popczun, J. R. McKone, C. G. Read, A. J. Biacchi, A. M. Wiltrout, N. S. Lewis, R. E. Schaak, *J. Am. Chem. Soc.* **2013**, *135*, 9267; b) E. J. Popczun, C. G. Read, C. W. Roske, N. S. Lewis, R. E. Schaak, *Angew. Chem. Int. Ed.* **2014**, *53*, 5427; c) X. Long, G. Li, Z. Wang, H. Zhu, T. Zhang, S.

This article is protected by copyright. All rights reserved.

- Xiao, W. Guo, S. Yang, *J. Am. Chem. Soc.* **2015**, *137*, 11900; d) W. Zhu, X. Yue, W. Zhang, S. Yu, Y. Zhang, J. Wang, J. Wang, *Chem. Commun* **2016**, *52*, 1486; e) H. Zhou, F. Yu, Y. Huang, J. Sun, Z. Zhu, R. J. Nielsen, R. He, J. Bao, W. A. Goddard III, S. Chen et al., *Nat. Commun.* **2016**, *7*, 12765; f) H. Vrubel, X. Hu, *Angew. Chem. Int. Ed.* **2012**, *124*, 12875.
- [10] Z.-H. Xue, H. Su, Q.-Y. Yu, B. Zhang, H.-H. Wang, X.-H. Li, J.-S. Chen, *Adv. Energy Mater.* **2017**, 1602355.
- [11] a) S. Zhao, Y. Wang, J. Dong, C.-T. He, H. Yin, P. An, K. Zhao, X. Zhang, C. Gao, L. Zhang et al., *Nat. Energy* **2016**, *1*, 16184; b) H. Liang, F. Meng, M. Caban-Acevedo, L. Li, A. Forticaux, L. Xiu, Z. Wang, S. Jin, *Nano Lett.* **2015**, *15*, 1421; c) Z. Lu, H. Wang, D. Kong, K. Yan, P.-C. Hsu, G. Zheng, H. Yao, Z. Liang, X. Sun, Y. Cui, *Nat. Commun.* **2014**, *5*, 4345; d) X. Han, C. Yu, S. Zhou, C. Zhao, H. Huang, J. Yang, Z. Liu, J. Zhao, J. Qiu, *Adv. Energy Mater.* **2017**, 1602148.
- [12] a) G. N. Glaviee, K. J. Klabunde, C. M. Sorensen, G. C. Hadjapanayis, *Langmuir* **1992**, *8*, 771; b) P. E. R. Blanchard, A. P. Grosvenor, R. G. Cavell, A. Mar, *Chem. Mater.* **2008**, *20*, 7081.
- [13] J. Schreieffels, *J. Catal.* **1980**, *65*, 195.
- [14] a) S. Carencio, D. Portehault, C. Boissière, N. Mézailles, C. Sanchez, *Chem. Rev.* **2013**, *113*, 7981; b) U. B. Demirci, P. Miele, *Phys. Chem. Chem. Phys.* **2010**, *12*, 14651; c) G. M. Arzac, T. C. Rojas, A. Fernández, *Appl. Catal., B* **2012**, *128*, 39.
- [15] J. Suntivich, K. J. May, H. A. Gasteiger, J. B. Goodenough, Y. Shao-Horn, *Science* **2011**, *334*, 1383.
- [16] G. P. Shveikin, A. L. Ivanovskii, *Russ. Chem. Rev.* **1994**, *63*, 711.
- [17] C. Tang, N. Cheng, Z. Pu, W. Xing, X. Sun, *Angew. Chem. Int. Ed.* **2015**, *54*, 9351.
- [18] a) M. Ledendecker, S. Krick Calderón, C. Papp, H.-P. Steinrück, M. Antonietti, M. Shalom, *Angew. Chem. Int. Ed.* **2015**; b) L.-A. Stern, L. Feng, F. Song, X. Hu, *Energy Environ. Sci.* **2015**, *8*, 2347; c) M. Shalom, D. Ressnig, X. Yang, G. Clavel, T. P. Fellingner, M. Antonietti, *J. Mater. Chem. A* **2015**, *3*, 8171; d) Y.-P. Zhu, Y.-P. Liu, T.-Z. Ren, Z.-Y. Yuan, *Adv. Funct. Mater.* **2015**, *25*,

This article is protected by copyright. All rights reserved.

- 7337; e) W. Zhou, X.-J. Wu, X. Cao, X. Huang, C. Tan, J. Tian, H. Liu, J. Wang, H. Zhang, *Energy Environ. Sci.* **2013**, *6*, 2921.
- [19] A. Maljusch, O. Conradi, S. Hoch, M. Blug, W. Schuhmann, *Anal. Chem.* **2016**, *88*, 7597.
- [20] S. Chen, J. Duan, P. Bian, Y. Tang, R. Zheng, S.-Z. Qiao, *Adv. Energy Mater.* **2015**, *5*, 1500936.
- [21] H. Liang, A. N. Gandi, D. H. Anjum, X. Wang, U. Schwingenschlogl, H. N. Alshareef, *Nano Lett.* **2016**, *16*, 7718.
- [22] B. Zhang, X. Zheng, O. Voznyy, R. Comin, M. Bajdich, M. Garcia-Melchor, L. Han, J. Xu, M. Liu, L. Zheng et al., *Science* **2016**, *352*, 333.
- [23] J. Masa, S. Barwe, C. Andronesco, I. Sinev, A. Ruff, K. Jayaramulu, K. Elumeeva, B. Konkena, B. Roldan Cuenya, W. Schuhmann, *ACS Energy Lett.* **2016**, *1*, 1192.
- [24] J. O. Bockris, T. Otagawa, *J. Phys. Chem.* **1983**, *87*, 2960.
- [25] S. Gul, J. W. D. Ng, R. Alonso-Mori, J. Kern, D. Sokaras, E. Anzenberg, B. Lassalle-Kaiser, Y. Gorlin, T.-C. Weng, P. H. Zwart et al., *Phys. Chem. Chem. Phys.* **2015**, *17*, 8901.
- [26] A. N. Mansour, *J. Electrochem. Soc.* **1994**, *141*, L69-L71.
- [27] M. Gorlin, P. Chernev, J. Ferreira de Araujo, T. Reier, S. Dresp, B. Paul, R. Krahnert, H. Dau, P. Strasser, *J. Am. Chem. Soc.* **2016**, *138*, 5603.
- [28] a) Y. Matsumoto, E. Sato, *Mater. Chem. Phys.* **1986**, *14*, 397; b) H. Dau, C. Limberg, T. Reier, M. Risch, S. Roggan, P. Strasser, *ChemCatChem* **2010**, *2*, 724.
- [29] J. Ferreira de Araujo, H. Schmies, D. Bernsmeier, S. Dresp, M. Gliech, Z. Jusys, P. Chernev, R. Kraehnert, H. Dau, P. Strasser, *J. Am. Chem. Soc.* **2017**, 2070.

This article is protected by copyright. All rights reserved.

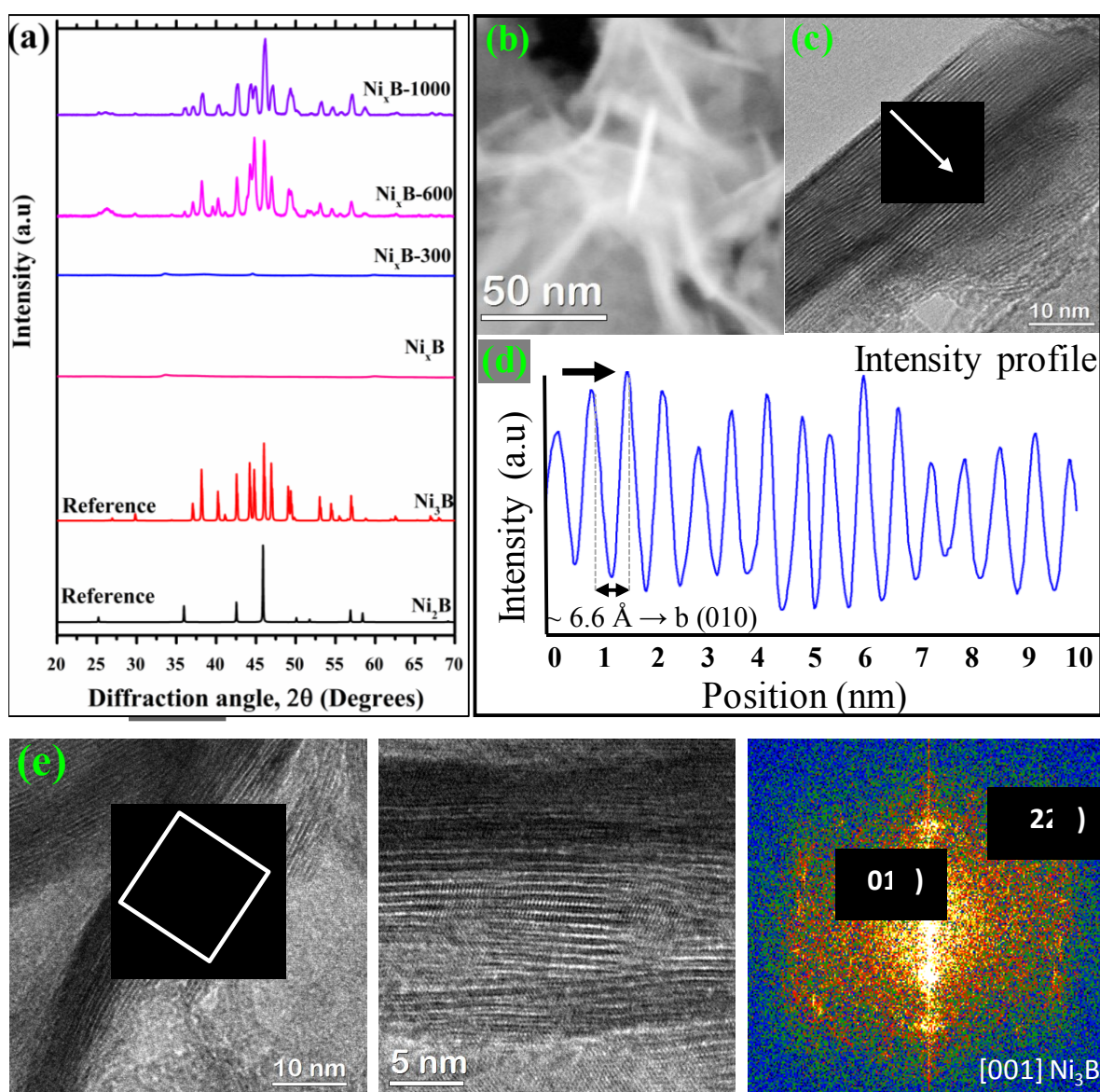


Figure 1. (a) XRD patterns of Ni_xB , Ni_xB annealed at 300 °C ($\text{Ni}_x\text{B-300}$), 600 °C ($\text{Ni}_x\text{B-600}$), and at 1000 °C ($\text{Ni}_x\text{B-1000}$), and of the references Ni_2B (ICSD 75792) and Ni_3B (ICSD 614985). (b) High-angle annular dark field (HAADF) low magnification TEM micrograph of $\text{Ni}_x\text{B-300}$, (c) HRTEM of a single flake showing layers of sheets, (d) intensity profile taken across the flake along the white arrow in (c) showing individual sheets with a thickness of ≈ 6.6 Å. (e) HRTEM image of $\text{Ni}_x\text{B-300}$ with a magnified view of the rectangular marked region and its corresponding FFT pattern.

This article is protected by copyright. All rights reserved.

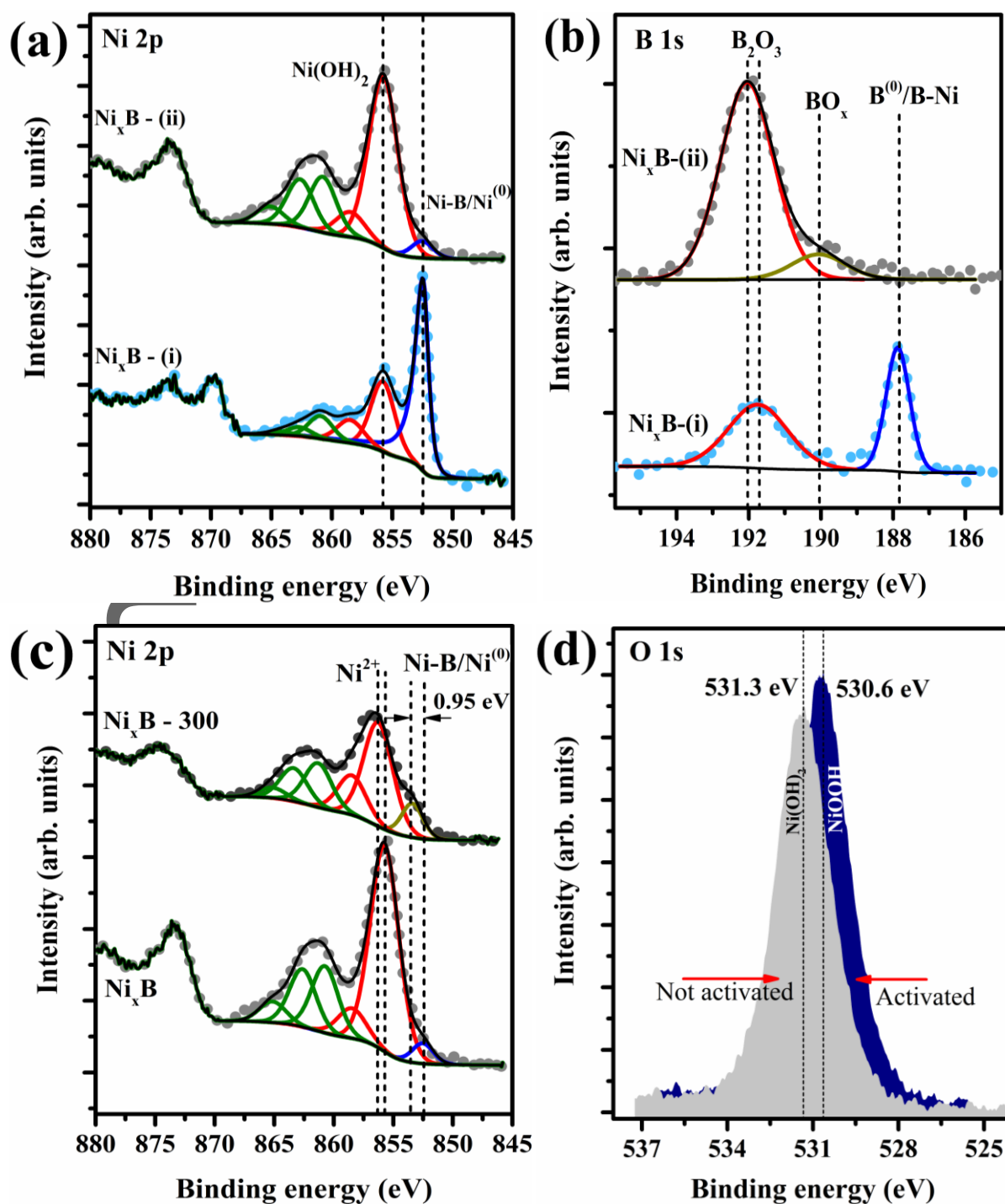


Figure 2. XPS analysis: (a) Ni 2p and (b) B 1s core-level spectra of Ni_xB minimally exposed to air (i) and after prolonged air exposure (ii). (c) Ni 2p core-level spectra of Ni_xB and Ni_xB after annealing

This article is protected by copyright. All rights reserved.

under argon at 300 °C, and (d) O 1s high-resolution spectra of Ni_xB-300 before and after electrochemical activation.

Author Manuscript

This article is protected by copyright. All rights reserved.

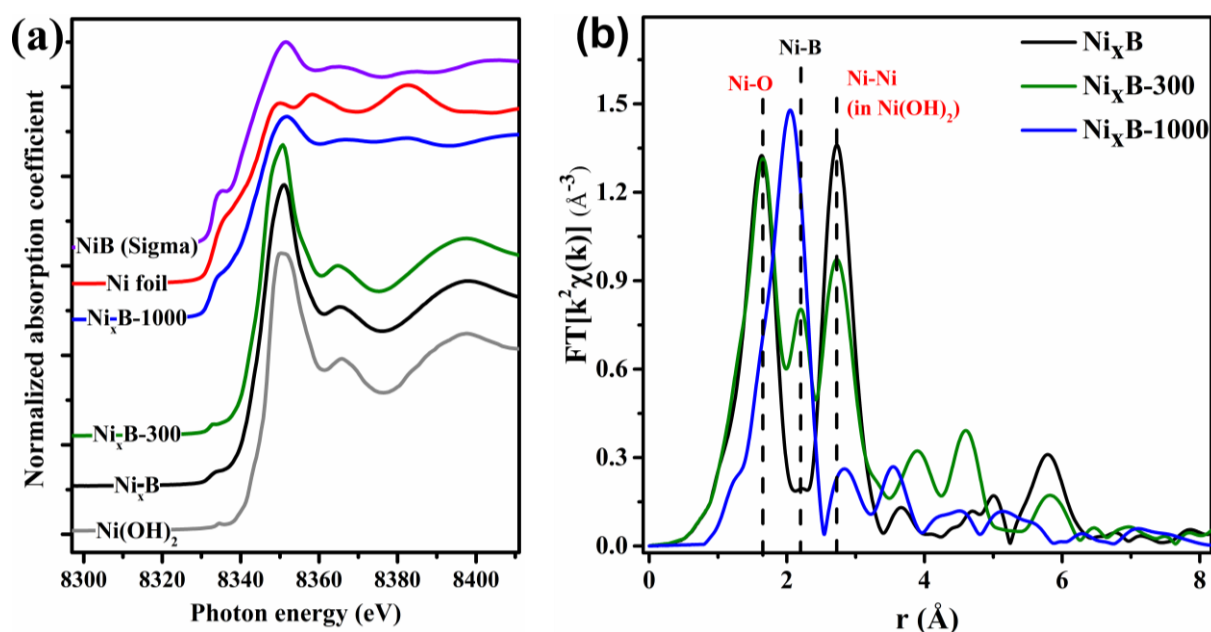


Figure 3. (a) X-ray absorption near-edge structure (XANES) spectra of the as prepared Ni_xB sample, Ni_xB annealed at 300 °C (Ni_xB-300) under argon, Ni_xB annealed at 1000 °C under argon (Ni_xB-1000), a Ni-foil, NiB (Sigma Aldrich) and Ni(OH)₂ as references. (b) Extended X-ray absorption fine structure (EXAFS) spectra of Ni_xB, Ni_xB-300, and Ni_xB-1000.

Author Manuscript

This article is protected by copyright. All rights reserved.

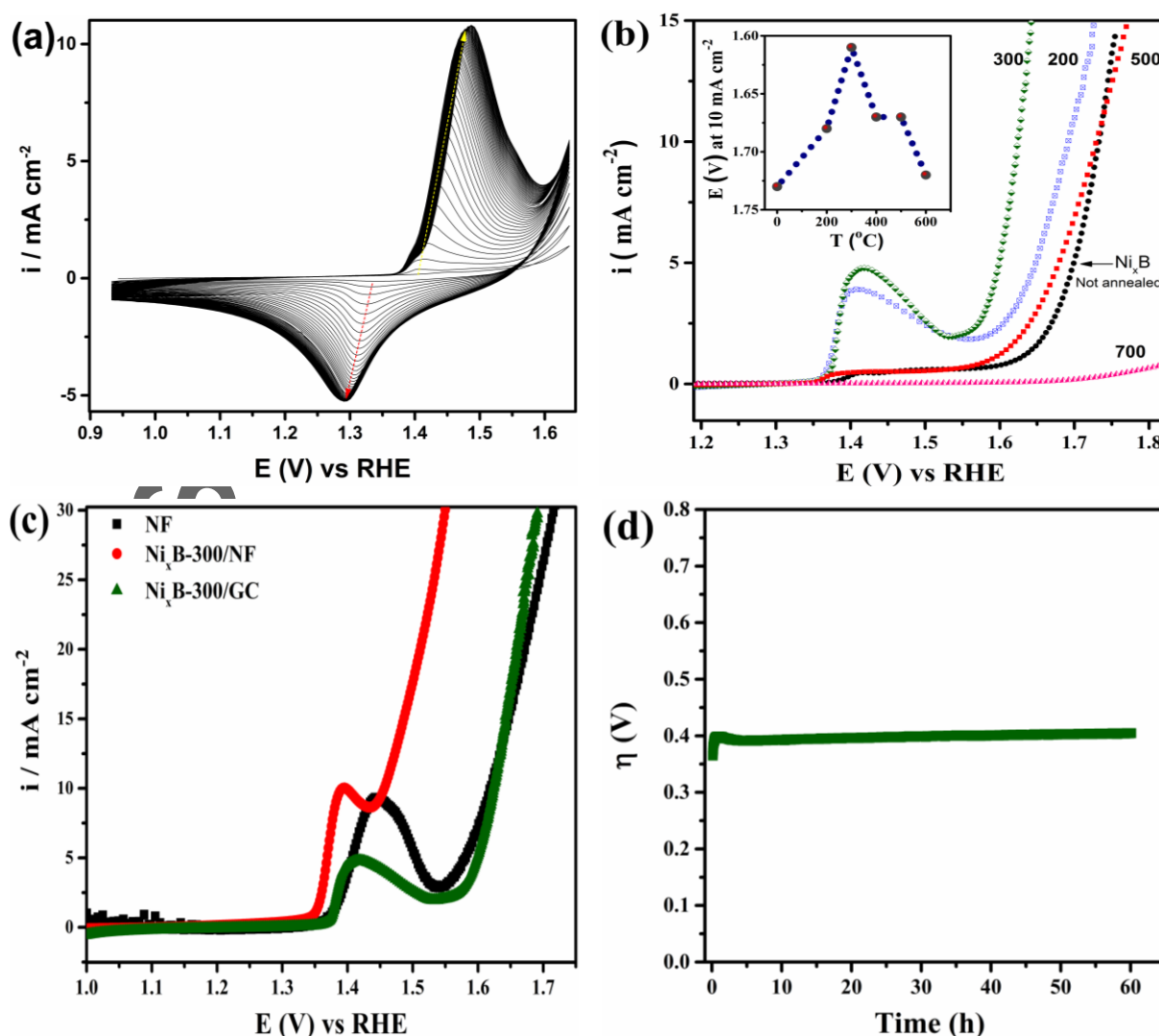


Figure 4. (a) Activation of Ni_xB by continuous potential cycling between 0.95 V and 1.65 V at 100 mV s^{-1} in 0.1 M KOH ; (b) Linear sweep voltammograms (LSVs), corrected for the resistance of the electrolyte, of Ni_xB and Ni_xB annealed at 200°C , 300°C , 500°C and 700°C , recorded at 10 mV s^{-1} in 0.1 M KOH and at 1600 rpm electrode rotation. Inset: variation of the OER activity of Ni_xB , expressed as the potential at a current density of 10 mA cm^{-2} , with annealing temperature. (c) Galvanostatic long-term stability measurement of Ni_xB -300 deposited on a graphite rotating disk electrode (Area = 0.196 cm^2) at 10 mA cm^{-2} in KOH (0.1 M); (d) comparative LSVs of a bare nickel foam (NF) electrode, and Ni_xB -300 supported on glassy carbon (Ni_xB -300/GC) and on nickel foam (Ni_xB @NF).

This article is protected by copyright. All rights reserved.

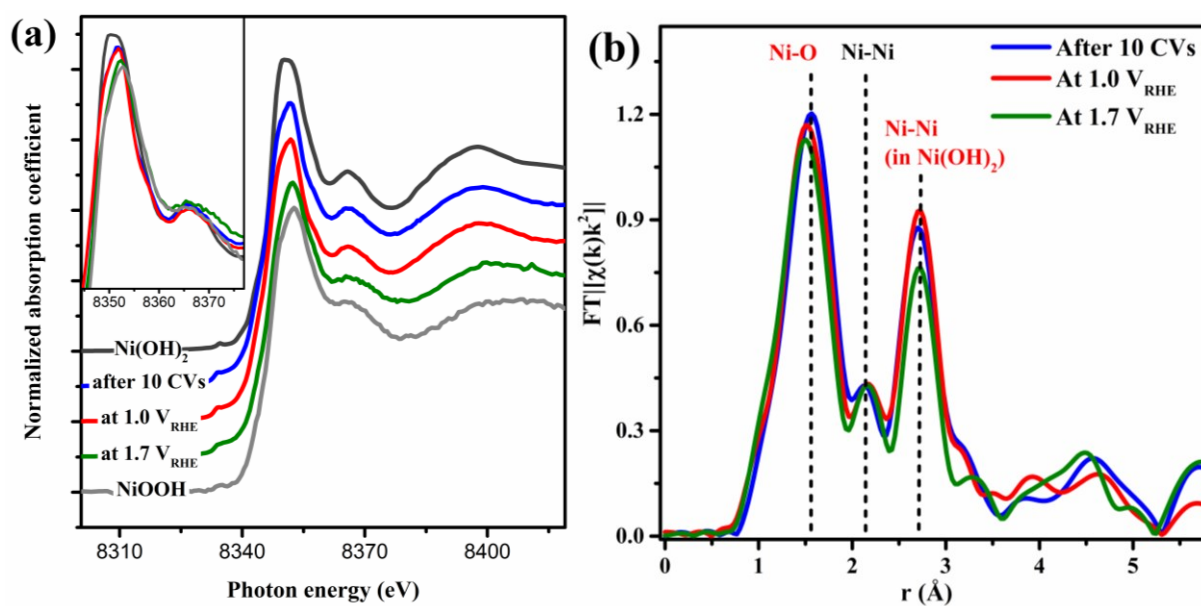


Figure 5. Operando XANES (a) and EXAFS (b) spectra of $\text{Ni}_x\text{B-300}$ acquired after conditioning (10 CVs) during OER at different electrochemical potentials, 1.0 V and 1.7 V versus RHE.

Author Manuscript

This article is protected by copyright. All rights reserved.

Ultrathin high-surface area nickel boride nanosheets supported on nickel foam show outstanding activity in catalyzing the oxygen evolution reaction, ranking among the best non-precious catalysts for oxygen evolution reported to-date.

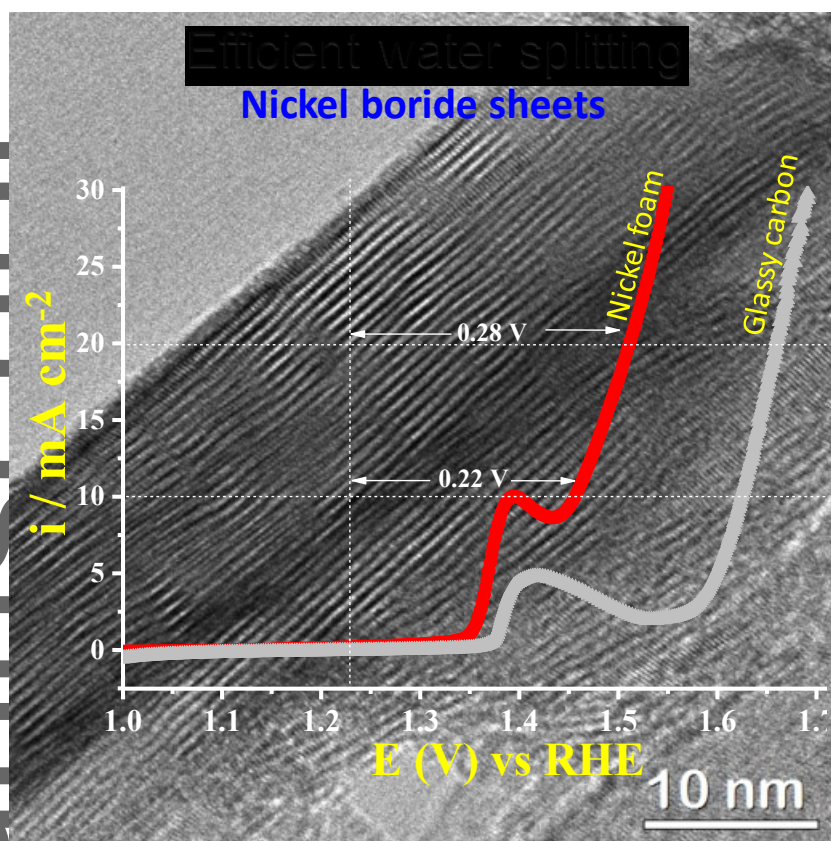
Water splitting

J. Masa^{a*}, I. Sinev, H. Mistry, E. Ventosa, M. Mata, J. Arbiol, M. Muhler, B. R. Cuenya^b, Wolfgang Schuhmann^{**}

Ultrathin high surface area nickel boride (Ni_xB) nanosheets as highly efficient electrocatalyst for oxygen evolution

Author Manuscript

This article is protected by copyright. All rights reserved.



This article is protected by copyright. All rights reserved.